DEVELOPMENT OF ENSEMBLE-BASED PROBABILISTIC FLOOD MAPS FOR PROBABLE MAXIMUM FLOOD

A report submitted to fulfill the research requirements of Hydro Research Foundation Fellowship

Sudershan Gangrade
May 31, 2018

Development of Ensemble-based Probabilistic Flood Maps for Probable Maximum Flood *

Sudershan Gangrade,[1,2,3] Shih-Chieh Kao,[1,2,3,*] Tigstu T. Dullo,[4] Alfred J. Kalyanapu,[4] and Benjamin L. Preston[5]

[1] The Bredesen Center, University of Tennessee, Knoxville, TN 37996, USA
[2] Environmental Sciences Division, Oak Ridge National Laboratory, Oak Ridge, TN 37831, USA
[3] Climate Change Science Institute, Oak Ridge National Laboratory, Oak Ridge, TN 37831, USA
[4] Department of Civil and Environmental Engineering, Tennessee Technological University, Cookeville, TN 38505, USA
[5] RAND Corporation, P.O. Box 2138, Santa Monica, CA 90407, USA

Table of Contents

104

105

106 **Abstract**

107 The magnitude and frequency of hydro-meteorological extremes are expected to increase in a

108 changing environment that threaten the security of US energy-water assets. This includes

109 probable maximum precipitation (PMP) and probable maximum flood (PMF) which are used as

110 hydraulic design standards for critical infrastructures such as major hydropower reservoirs and

111 nuclear power plants. To assess the potential flood hazards due to PMP/PMF, an integrated high-

112 resolution process-based hydro-meteorologic modeling framework was utilized to develop

113 ensemble-based probabilistic flood maps based on best-available historic observations and future

114 climate projections. A graphical process unit accelerated 2-dimensional hydrodynamic model

115 was used to simulate the surface inundation areas corresponding to a total of 120 PMF

116 hydrographs. These ensemble-based PMF maps were compared with flood maps obtained from

117 the conventional deterministic PMP/PMF approach, revealing added information of conditional

118 probability of flooding. Further, a relative sensitivity test was conducted to explore the effects of

119 various factors in the framework such as meteorological forcings, antecedent hydrologic

120 conditions, reservoir storage, and flood model input resolution and parameters. The proposed

121 framework better illustrates the uncertainties associated with model inputs, parameterization and

122 hydro-meteorological factors allowing more informed decision-making for future emergency

123 preparation.

1. Introduction

Floods are one of the most destructive natural hazard causing deaths and damages to infrastructures worldwide. The United States (US) alone has observed 29 billion-dollar scale flood events in the period of 1980–2018 with a total of 543 deaths and roughly 122 billion dollars inflation adjusted loss (NCEI, 2018). The increasing frequency and magnitude of flood events under a changing climate, land use land cover and population require better predictability and preparedness towards flood hazards. The flood inundation maps serve as a critical input to flood risk assessments and enable development of informed floodplain management and mitigation strategies. In the US, Federal Emergency Management Agency (FEMA) utilize hydrologic and hydraulic models to delineate flood inundation zones associated with 1% and 0.2% annual exceedance probability (AEP) (or 100-year and 500-year return period) to support the National Flood Insurance Program (FEMA, 2018). For critical energy-water infrastructures including major hydropower dams and nuclear power plants, the even rarer events (AEP < 0.2%) or probable maximum flood (PMF) are the focus. Similar inundation maps developed for PMF-scale events may serve as a useful tool to evaluate the vulnerability of critical infrastructures under the worst case flooding scenario, as well as to identify regions with minimum flooding likelihood to support future site selection.

A general procedure to prepare flood inundation maps (hereinafter referred as "modeling chain") associated with PMF involves: probable maximum precipitation (PMP) estimation, followed by hydrologic simulation, and hydrodynamic/hydraulics modeling. Since the current practice of PMP/PMF assessment focuses on estimating the single deterministic maximum precipitation and streamflow event (that could occur under a series of adverse hydro-meteorological conditions), the conventional PMF inundation maps are also deterministic in

149   nature. However, deterministic maps would inevitably refrain the decision makers or planners

150   from the underlying uncertainties, given the binary (wet or dry) representation of the resulting

151   flood inundation maps. While the advanced deterministic maps employ process based hydrologic

152   and hydraulics model calibrated to historic events (Di Baldassarre et al., 2010), these maps are

153   unable to capture the uncertainties arising from various sources in the modeling chain such as

154   inaccurate input data, boundary conditions, model structure, and model parameterization

155   (Alfonso et al., 2016; Di Baldassarre et al., 2010). Therefore, the values and potential of

156   probabilistic flood maps (PFMs) are now highlighted (Alfonso et al., 2016; Di Baldassarre et al.,

157   2010; Papaioannou et al., 2017). Recent advances in computational power has allowed the use of

158   computationally intensive hydrologic-hydraulics models to develop PFM through multi-

159   ensemble simulation (Neal et al., 2013). The uncertainty characterization may be performed at

160   various stages of modeling chain by varying factors such as precipitation (Caseri et al., 2016),

161   spatiotemporal rainfall variability (Jenkins et al., 2017; Nuswantoro et al., 2016; Zischg et al.,

162   2018), spatial dependence of flow from tributaries (Neal et al., 2013; Pattison et al., 2014),

163   hydrologic model parameters or inputs (Domeneghetti et al., 2013), hydraulic model types

164   (Papaioannou et al., 2016), hydraulic model roughness coefficient (Papaioannou et al., 2017),

165   and different digital elevation models and observational data sets (Giustarini et al., 2016;

166   Papaioannou et al., 2016).

167   While a few studies have focused on the development of flood inundation maps for the

168   largest historic events (e.g., Pedrozo-Acuña et al., 2015) or for events with return period ranging

169   from hundreds (Smemoe et al., 2007) to thousands of years (Büchele et al., 2006; Prime et al.,

170   2016), studies evaluating flood inundation maps for rare hydroclimate extreme events such as

171   PMP/PMF are limited (Zischg et al., 2018). Further, recent studies have suggested the sensitivity

172   of PMP/PMF in a warming environment (e.g., Kunkel et al., 2013; Beauchamp et al., 2013;

173   Rousseau et al., 2014; Stratz and Hossain, 2014; Klein et al., 2016; Rastogi et al., 2017;

174   Gangrade et al., 2018) and challenged the deterministic treatment of PMP/PMF. It has also been

175   suggested that both epistemic and aleatoric uncertainties involved in the estimation of PMP

176   (Micovic et al., 2015). For instance, PMP and PMF estimates are often derived for a point

177   location of interest without considering variability originating from spatiotemporal rainfall

178   distribution or watershed heterogeneity. Through Monte Carlo simulation, Zischg et al. (2018)

179   demonstrated that the spatiotemporal distribution of PMP has significant effects on the resulting

180   PMF inundation maps. Other factors such as antecedent soil moisture, meteorological forcings,

181   land use landcover and reservoir operation (Gangrade et al., 2018) may introduce further

182   uncertainties to the estimated PMF and consequently the resulting surface inundation area.

183   Moving forward, it is of critical importance to advance our concept and practice from the

184   conventional, deterministic treatment of PMP/PMF to an ensemble-based, probabilistic flood

185   mapping approach to better analyze and quantify the vulnerability of critical energy-water

186   infrastructures in a changing environment.

187   In this study, building upon our prior works on PMP/PMF simulations (Rastogi et al., 2017;

188   Gangrade et al., 2018), we present a high-resolution, process-based, hydro-meteorological

189   modeling framework to produce probabilistic flood inundation maps for PMF. The main

190   objectives of the study are: (1) employ an ensemble-based approach to translate uncertainties

191   associated with PMP to flood inundation maps, (2) prepare flood inundation probability maps

192   illustrating uncertainties associated in the flood hazard modeling chain for PMF, and (3) quantify

193   the potential impacts of environmental change on the inundation areas of PMF. The study area

194   includes areas immediately upstream and downstream of the second largest dam (by maximum

195 storage capacity in Alabama Coosa Tallapoosa River Basin), Allatoona Dam, in Georgia, US.

196 For PMP, we used an ensemble of 120 storms simulated by the Weather Research Forecasting

197 model (WRF; Skamarock et al., 2008), driven by both reanalysis and climate projection forcings

198 using the approach as described by Rastogi et al. (2017). These PMP storms were then used to

199 simulate PMF through a high resolution Distributed Hydrologic Soil Vegetation Model

200 (DHSVM; Wigmosta et al., 1994) as described in Gangrade et al. (2018). The ensemble of PMF

201 hydrographs was further used to drive a high-resolution, Graphics Processing Unit (GPU)

202 accelerated 2-dimensional dynamic wave flood model (Flood2D-GPU; Kalyanapu et al., 2011)

203 to simulate the spatiotemporal evolution of PMF and to develop the ensemble-based probabilistic

204 flood maps. Apart from better showing uncertainties (as opposed to the deterministic approach),

205 the ensemble-based flood mapping approach allows us to better visualize the potential impacts of

206 PMF through a more intuitive manner. The study also includes a relative sensitivity experiment

207 to evaluate the sensitivity of various factors in the modeling chain including inputs such as

208 precipitation, hydrologic model antecedent conditions, and hydraulic model parameters.

209   This paper is structured as follows: Section 2 introduces the overall method, data, and study

210 area; Section 3 illustrates and describes results; and Section 4 presents a summary and the

211 conclusion of this study.

212 **2. Methods**

213 **2.1   Study Area**

214   Our study area consists of Etowah watershed, located in northwestern Georgia, United States.

215 The Etowah watershed is an eight-digit hydrologic unit (HUC08) with an approximate drainage

216 area of 4821 km^2 (1861 mi^2; Figure 1) and is a part of Alabama-Coosa-Tallapoosa River Basin.

217 It drains parts of 15 counties of Georgia with major urban areas including city of Cartersville and

218   Atlanta's metropolitan areas such as Woodstock, Marietta and Alpharetta. The Etowah

219   watershed includes a large multi-purpose reservoir, Allatoona Lake and Dam, owned and

220   operated by the United States Army Corps of Engineers (USACE), with a maximum storage

221   capacity of roughly 826.5 million m^3. While the headwaters of Etowah Watershed include

222   mountainous areas (such as Piedmont mountains), the topography of the rest of the watershed is

223   moderate with the elevation ranges from ~176 m (577 ft) to 1,147 m (3,763 ft) based on the

224   United States Geological Survey (USGS) National Elevation Dataset (NED; Gesch et al., 2002).

225   The region receives precipitation of roughly 1,336 mm per year predominantly in the form of

226   rainfall, with light snowfall in the headwater region. The major soil types include sandy loam

227   and silty loam. As per National Land Cover Database (NLCD), 61% of the basin is covered by

228   forests, 18.5 percent under small vegetation, and 18.5 percent fall under developed category.

229   [Figure 1]

230   The meteorological and hydrologic simulations were conducted for the entire Etowah

231   Watershed, while the flood (hydraulic) simulations were conducted for two selected regions

232   upstream (ME01) and immediate downstream (ME02) areas of Allatoona Dam (Figure 1). These

233   areas were selected such that it includes urban areas of Atlanta metropolitan area and city of

234   Cartersville. The computational domains for Flood2D-GPU for both regions ME01 and ME02

235   are larger than the area of interest, with corresponding area of 358 km^2 and 507 km^2. The

236   computational domains are selected larger than the area of interest to avoid any potential

237   backwater effects and computational domain boundary artefacts.

238   **2.2   Modeling Framework**

239   This study utilizes an ensemble based, high-resolution process-based modeling framework to

240   develop flood inundation maps associated with probable maximum flood estimates. The main

9

241   steps involve 1) simulation of PMP 2) simulation of PMF hydrographs and, 3) simulation of

242   PMF flood maps. A brief overview is provided below:

243   **2.2.1   Simulation of PMP**

244   The PMP simulation was performed for an ensemble of 120 moisture-maximized storms by

245   Rastogi et al. (2017) using a WRF version 3.6, a mesoscale numerical weather model, running

246   using a double two-way nested domain at 9 km and 3 km horizontal spacing. The boundary

247   forcings for WRF simulations included both Climate Forecast System Reanalysis I (CFSR; Saha

248   et al., 2010) and Community Climate System Model version 4 (CCSM4; Gent et al., 2011). The

249   storms include four sets:

250   (1) **CFSR-CT**: Controlled simulation that includes the 30 largest historic storms during the

251   1981–2011 historic period driven by CFSR reanalysis.

252   (2) **CCSM4-BL**: Baseline simulation that includes the 30 largest storms driven by both

253   1981–2005 in the historical period and 2006–2010 in a future period under an RCP8.5

254   scenario of CCSM4 experiments.

255   (3) **CCSM4-F1**: Near-future simulation that includes the 30 largest storms driven by a 2021–

256   2050 CCSM4 projection under an RCP8.5 scenario.

257   (4) **CCSM4-F2**: Far-future simulation that includes the 30 largest storms driven by a 2071–

258   2100 CCSM4 projection under an RCP 8.5 scenario.

259   The Relative Humidity Maximization method (RHM; Ohara et al., 2011; Ishida et al., 2015)

260   that adjusts relative humidity in the boundary conditions of the entire atmospheric column to

261   100% (i.e., fully saturated) was then used to simulate moisture-maximized storms to derive PMP.

262   Prior to PMP generation, the WRF simulations were extensively evaluated against both Oregon

263   State University's PRISM (Daly et al., 2008) and Oak Ridge National Laboratory's (ORNL)

264   Daymet (Thornton et al., 1997) gridded precipitation data sets to select most appropriate

265   parameterization scheme. The readers are referred to Rastogi et al. (2017) for further technical

266   details regarding PMP estimation and WRF performance evaluation.

267   In addition, conventional PMP rainfall estimates were obtained using HMR51 and HMR52 to

268   provide a reference and enable comparison of ensemble-based simulations with conventional

269   deterministic approach. The conventional approach requires conversion of depth-area-duration

270   table to generate spatiotemporal storm hyetograph, after a deterministic PMP depth is chosen. In

271   this study, we use spatial hourly precipitation grid as an input for hydrologic simulation which

272   allows to capture the spatial structure of each storm. A key difference between the ensemble

273   approach and conventional PMP estimate relies in identifying the most critical PMF event based

274   on hydrologic and hydraulic simulations for each of the moisture-maximized storm as opposed to

275   one deterministic event based on synthetic hyetograph. The ensemble-based approach allows to

276   help us better understand the uncertainty associated with PMP estimates.

277   **2.2.2   Simulation of PMF**

278   The PMF simulations were conducted by using each of the 120 storms mentioned in Section

279   2.2.1 as an input meteorological forcing to a high resolution distributed hydrologic model known

280   as distributed hydrology soil vegetation model (DHSVM). The hydrologic model was selected

281   due to its previous applications in studying climate change impacts on streamflow extremes and

282   ability to provide high resolution output (e.g., streamflow at each channel in the stream network)

283   which serves as a key input to drive flood model. DHSVM performs mass (water) and energy

284   balance calculations at each grid cell and accounts for hydrological processes such as

285   evapotranspiration, snowmelt, canopy snow interception and release, unsaturated soil moisture,

286   saturated subsurface flow, overland flow, and channel flow. The spatially distributed parameters

11

287   include topography, soil, and vegetation. The model requires a set of meteorological inputs that

288   includes precipitation, shortwave and longwave radiation, relative humidity, wind speed, and air

289   temperature. A detailed description of DHSVM can be found in Wigmosta et al. (1994 and 2002)

290   and Storck et al. (1998).

291   The DHSVM setup for Etowah Watershed was obtained from Gangrade et al. (2018) which

292   is a part of a much larger modeling effort performed for a HUC04 region i.e. Alabama-Coosa-

293   Tallapoosa River Basin. A brief description of the DHSVM setup is provided below. The readers

294   are referred to Gangrade et al. (2018) for associated detailed technical description regarding

295   setup, calibration and validation. The DHSVM was setup at a fine 90-m horizontal grid

296   resolution at 3-h time steps from 1980 to 2012, using 1980 for model spin-up. A 90-m resolution

297   digital elevation model (DEM) was resampled from the 30-m resolution NED for Etowah

298   Watershed. The DEM serves as the base map and additional datasets including soil depth, soil

299   type, and LULC type, were obtained at the same resolution of DEM. The stream network was

300   obtained from the National Hydrography Dataset Plus (NHDPlus; McKay et al., 2012) for

301   accurate representation of channels in the study area. The soil data was obtained from a

302   multilayer contiguous US soil characteristics data set (Miller and White, 1998) derived from the

303   State Soil Geographic Database (Schwarz and Alexander, 1995). A set of soil-hydraulic

304   properties such as porosity, hydraulic conductivity, wilting point, bubbling pressure, and field

305   capacity were assigned to every soil texture type (Maidment, 1993) for the dominant soil texture

306   type at each grid cell. The LULC map was obtained from the USGS National Land Cover

307   Database 2006 (NLCD; Fry et al., 2011). A set of vegetation properties including leaf area index,

308   albedo, stomatal resistance, moisture threshold, and fractional coverage were assigned to every

309   land cover type.

12

310   The PMF was obtained by employing the concept of meteorologically transpositionable

311   storms to identify the most critical PMP input for the Etowah Watershed. Due to an overall

312   smooth topography in the southeast United States, this approach allows to identify the most

313   intense portion of a storm and transposition it over the desired study area. As a result, depending

314   on the size and shape of a selected watershed, the transpositioned PMP storm inputs may be

315   different. For each of the 120 moisture-maximized storms (as described in Section 2.2.1), the

316   largest 72 hr average precipitation over the watershed was identified and transpositioned re-

317   gridded to the same 4 km DHSVM radar rainfall format used for DHSVM calibration and

318   validation. In addition, the WRF output also provides shortwave and longwave radiation,

319   humidity, and other required DHSVM meteorological inputs. As per the NRC guidelines (Prasad

320   et al., 2011), a meteorological sequence that included 40% of PMP in the first 72 h (antecedent

321   precipitation), followed by 72 h of no precipitation, and then 72 h of full PMP (critical

322   precipitation) was used as the default setup to simulate PMF. The fully saturated moisture

323   conditions were utilized at the beginning of DHSVM simulations. The simulation was continued

324   for another 6 days to ensure the capture of peak flood hydrographs. This approach provides an

325   ensemble of simulated DHSVM streamflow hydrographs for each set of storms (CFSR-CT,

326   CCSM4-BL, CCSM4-F1, and CCSM4-F2).

327   To compare the results with conventional PMF, PMP rainfall inputs were also calculated for

328   Etowah Watershed using HMR51 and HMR52. The 72-h HMR PMP hyetograph was computed

329   using a critically stacked temporal pattern, which was used to drive the DHSVM simulation. The

330   critically stacked pattern allowed the occurrence of PMP for all durations (e.g., 1, 6, 12, 24, 48,

331   72 h) within a single storm of 72-h duration to generate a high-intensity storm (HMR52).

332

2.2.3 Flood Modeling

333   **2.2.3   Flood Modeling**

334   The flood simulation for this study was performed using the computationally enhanced

335   version of the 2D hydraulic model Flood2D-GPU (Marshall et al., 2017), originally developed

336   by Kalyanapu et al. (2011). The numerical algorithm in Flood2D-GPU utilize a first-order

337   accurate upwind finite difference scheme that solves the non-linear hyperbolic shallow water

338   equations (SWE) (Saint Venant Equations). These equations are simplified version of the

339   Navier-Stokes equations, where the horizontal momentum and continuity equations are

340   integrated over depth. The numerical model implements a structured grid to take advantage of

341   the uniform grid structure of the DEM data. Flood2D-GPU has the capability to use a spatially

342   varying surface roughness coefficient (Manning's n value), which can be obtained from a

343   standard table for a given land cover data (Phillips and Tadayon, 2007). The computational

344   performance of the Flood2D-GPU model was improved using a hybrid MPI+CUDA architecture.

345   The model speed up for the MPI + multiple Graphics Processing Unit (GPU) version was up to

346   18x when compared to an identical single-process Open Multi-Processing (OpenMP) version

347   (Marshall et al., 2017). The high performance of the model therefore allows to perform an

348   ensemble simulation for two domains ME01 (~400,000 grid cells, 360 sq. km) and ME02

349   (~563,000 grid cells, 507 sq. km). The simulations were conducted on Titan supercomputer

350   maintained by the Oak Ridge Leadership Computing Facility at Oak Ridge National Laboratory.

351   The key input data required for Flood2D-GPU model are terrain data, surface roughness

352   (Manning's n value), inflow source locations and corresponding flow hydrographs. In this study,

353   the 30m resolution DEM data is obtained from NED and a constant Manning's n value (0.035) is

354   utilized to setup the Flood2D-GPU. The inflow locations (Figure 1) are defined at the end of the

355   channel segments obtained from NHDPlus network. The corresponding hydrographs for each

356 120 storms are extracted from the high-resolution hydrologic outputs from DHSVM (Section

357 2.2.2) at three hourly time-step for both domains, i.e., ME01 and ME02. Since, the DHSVM

358 outputs cumulative flow for each channel location, a post hydrologic-simulation water balance

359 correction was applied to estimate incremental flow hydrographs for locations when required.

360 The Flood2D-GPU performance is evaluated and presented in later section (please see Section

361 3.1). The flood model output was stored at a 10-minutes interval for each storm. The current

362 model setup allows to capture riverine or fluvial floods, the pluvial flood simulation capabilities

363 will be incorporated in the future model improvements.

364 An additional set of 120 flood simulations were conducted for ME02 to account for the

365 reservoir operation effects in a rudimentary way. Since DHSVM setup in this study do not

366 account for reservoir presence in the watershed, a post-hydrologic simulation correction was

367 performed to adjust PMF hydrograph immediately downstream of Allatoona Lake and Dam. The

368 correction involved subtracting a water volume equivalent to the maximum storage capacity of

369 the Allatoona reservoir, i.e., 826.5 million m^3 from the peak portion of the PMF hydrograph. This

370 corrected hydrograph in addition to natural flow from other tributaries serve as an input to ME02

371 to drive Flood2D-GPU for each of the 30 storm sets from CFSR-CT, CCSM4-BL, CCSM4-F1

372 and CCSM4-F2.

373 This correction provided a maximum possible flood mitigation in terms of flood inundation

374 extents for the immediately downstream areas, under a best-case ideal flood management

375 scenario, which assumed a perfect PMF prediction and completely empty reservoirs at the

376 beginning of the PMF event. While actual reservoir operation will be different and more

377 complex, this assessment can aid understanding of the maximum PMF retention capacity of the

378 existing reservoirs and its impacts on flood mitigation.

379   **2.3   Probabilistic Flood Mapping**

380   For each storm's flood simulation (realization), the Flood2D-GPU simulation outputs were

381   post processed to obtain a binary wet-dry map where for each grid cell the distinction was made

382   by evaluating the flood depths (i.e. dry: flood depth equal zero, and wet was characterized as

383   flood depth greater than zero).

384   This results in a map of flood inundation extent for each realization. The probabilistic value

385   of flooding for any given cell was then calculated by weighing each storm equally using

386   Equation 1. This approach was utilized to produce one probabilistic flood map for each of the

387   storm sets i.e. CFSR-CT, CCSM4-BL, CCSM4-F1 and CCSM4-F2, for both ME01 and ME02.

388   In addition, probabilistic flood inundation maps were also generated for ME02 under reservoir

389   operation.

390   $$P_{cell} = \frac{\sum_{i=1}^{i=N} X_i}{N}$$ Equation 1

391   Where,

392   P_{cell} = probability to flood for any given cell

393   X_i = 0 (dry) or 1(wet) for realization 'i'

394   N = total number of realizations/flood event simulations

395   These probability values can then be presented as a spatial map of conditional probability of

396   flooding given a PMF event has occurred for the region of interest. The probabilistic flood maps

397   were generated for two model domains ME01 and ME02 for each of the 30 storm sets for CFSR-

398   CT, CCSM4-BL, CCSM4-F1 and CCSM4-F2. The flood simulations are referenced by adding

399   the subscript ME01, ME02 and ME02R after the name of storm set. For example, CFSR-CT-

400   ME01, CFSR-CT-ME02 and CFSR-CT-ME02R refers to probabilistic flood maps generated for

401 CFSR-CT storms for model domain ME01, ME02 under natural flow, and ME02 under reservoir

402 regulation respectively.

3. Results and Discussion

3.1 Flood2D-GPU Performance

405   The Flood2D-GPU performance is evaluated by comparing a simulated 1 in 100-year event

406 flood map against equivalent flood zones (Zone A / Zone AE) obtained from FEMA. This

407 approach captures the spatial extents of flood inundation obtained from simulation and compare

408 it with a benchmark dataset. It has been recently adopted to validate a hydrodynamic model for

409 conterminous US (Wing et al. 2017) and others (Alfieri et al. 2014). The model validation has

410 been performed for model domain ME01. The first step in the process involves estimation of a

411 100-year streamflow value. It was computed by conducting a standard flood frequency analysis

412 at the outlet of the ME01 using guidelines from Bulletin 17B prepared by Interagency Advisory

413 Committee on Water Data (1982). The continuous streamflow data from the control simulation

414 (i.e., DHSVM driven using observed historic precipitation from Daymet) was obtained for a

415 period of 32 years (1981–2012) which serves as an input for flood frequency analysis. A series

416 of annual maximum discharge was extracted from the hydrograph data. A log Pearson Type III

417 (LP3) distribution is then fit to a series of annual maximum discharge, using a skewness

418 parameter obtained for the region based on Plate 1 of Bulletin 17B. The results from the flood

419 frequency analysis are presented in Figure 2.

420   [Figure 2]

421   We employ an ensemble-based approach to validate the Flood2D-GPU, as a single storm

422 may not be able to capture the spatial-variability in the streamflow and may result in

423 underestimation of the flood extents for some channels. The hydrographs were extracted for each

17

424 of the inflow locations (Figure 1) capturing each of the annual maximum discharge (32 events

425 from 1981-2012). These hydrographs were then scaled to match the peak discharge to a 100-year

426 flood event discharge (i.e., 18950 cfs at outlet of ME01, Figure 2) which served as an input to

427 Flood2D-GPU. The ensemble simulation results in 32 flood inundation maps. The maximum

428 inundation area is then selected from the 32 maps and compared against FEMA 100-year flood

429 map rasterized to a 30 m resolution. The flood maps are compared based on a binary (flooded=1,

430 not-flooded = 0) classification scheme as presented in Table 1. The comparison is performed

431 exclusively for the region located downstream of the inflow locations. The vector-based flood

432 extents for the region of interest were rasterized to Flood2D-GPU grid to enable a direct

433 comparison.

434   [Table 1]

435   Figure 3 presents a comparison of flood inundation extents obtained from Flood2D-GPU and

436 FEMA for 100-year flood event. The regions where Flood2D-GPU accurately predicts the

437 FEMA flood zones are presented in blue. The region with overprediction (i.e. only flooded by

438 Flood2D-GPU but not FEMA) are presented in red, while the regions with underprediction (i.e.

439 flooded by FEMA but not captured by Flood2D-GPU are presented in green. The FEMA zones

440 excluded from this evaluation due to model or other data limitations are presented in grey. The

441 visual inspection reveals that Flood2D-GPU accurately predicts most of the FEMA flood zones.

442   [Figure 3]

443   The four key metrics to demonstrate model performance include hit rate (H), false alarm (F),

444 critical success (C) and error (E) (Table 2). The hit rate (H) provides a measure of model to

445 accurately predict the benchmark flood extents, however does not penalize for overprediction.

446 Flood2D-GPU obtained a H=0.82 for ME01 revealing that model can accurately predict 82% of

447   the FEMA flood zones. False alarm (F) that measures overprediction is estimated as 0.15,

448   demonstrating that 15% of the grid cells are falsely reported as flooded by the model. The critical

449   success (C) equivalent to the F squared statistics, a common metric to evaluate spatial extents for

450   flood studies (Bates and De Roo 2000), is estimated as 0.71 providing an overall measure of fit.

451   The C metric adds a penalty to H for any overprediction and underprediction. In addition, the

452   error value (E) for Flood2D-GPU being less than one (0.78) suggests an overall tendency of

453   model to underpredict which predominantly occurs in the upstream reaches close to inflow

454   boundary conditions.

455   [Table 2]

456   These key metrics reveal that Flood2D-GPU performance is at par to the acceptable range of

457   these metrics provided in the literature (Alfieri et al. 2014, Wing et al. 2017). For instance,

458   Alfieri et al. (2014) obtained H values between 0.59-0.78, and C values between 0.43-0.65 for a

459   flood simulation at a 100 m resolution across selected areas in Germany and UK compared with

460   national/regional hazard maps. Wing et al. (2017) performed a similar evaluation for validation

461   of flood hazard model for conterminous US using FEMA flood zones as benchmark, with a H

462   value as 0.685 and 0.815, and C value of 0.55 and 0.50 for a 90m and 30m resolution

463   respectively. The results indicate an overall satisfactory performance of the Flood2D-GPU in

464   comparing spatial extents for 1 in 100-year event against equivalent flood inundation zone

465   obtained from FEMA.

466   **3.2   Ensemble PMF Hydrographs and Comparison with Deterministic Approach**

467   This section presents the ensemble PMF hydrographs for each of the four storm sets (i.e.,

468   CFSR-CT, CCSM4-BL, CCSM4-F1 and CCSM4-F2) at the outlet of the Etowah Watershed

469   (Figure 4). The hydrographs resulting in the largest peak discharge are marked in thick lines and

19

470   are individually presented in Figure 5a. For further comparison, the PMF hydrograph from the

471   conventional approach (HMR based) is also presented for the Etowah Watershed (Figure 5a).

472   The range of peak discharge values for these events is presented in Figure 5b for Etowah

473   watershed and at the outlet of computational Flood2D-domains ME01 and ME02 in Figure 5c

474   and 5d respectively.

475   [Figure 4]

476   [Figure 5]

477   The results indicate that peak discharges obtained for CCSM4-BL and HMR are comparable

478   in magnitude with a maximum peak discharge value of 21,874 m^3/s and 18,654 m^3/s. The

479   maximum peak discharge for CFSR-CT (27,732 m^3/s) is greater as compared to that for CCSM4-

480   BL. This higher discharge could be attributed to higher PMP estimates for CFSR-CT,

481   demonstrating the effect of choice of meteorological forcings on PMF. The effects of climate

482   change on maximum peak discharge indicate a significant increase in peak discharge magnitude

483   with an increase of approximately 58% for near future time period (CCSM4-F1; 2021-2050), and

484   109% for far-future time period (CCSM4-F2;2071-2100). The comparison is performed with

485   reference to peak discharge magnitude obtained for the baseline period CCSM4-BL. These

486   changes could be directly attributed to increased projected PMP estimates in future periods

487   resulting from intensification of hydrologic cycle caused by strong atmospheric warming.

488   Readers are referred to Rastogi et al. (2017) and Gangrade et al. (2018) for further technical

489   details.

490   The results for Etowah Watershed demonstrate a large variability in the hydrograph shapes

491   and peak discharge values (Figure 5b), also observed for ME01 and ME02 (Figure 5c and 5d). In

492   addition to the key factor i.e. PMP magnitude, the variability in the hydrographs can also be

493   attributed to spatiotemporal rainfall structure and watershed heterogeneity. The results highlight

494   the range of uncertainties captured in terms of streamflow estimates which are often missing in

495   the conventional deterministic PMF estimation.

496   **3.3   Development of Probabilistic Flood Maps**

497   An ensemble approach provides multiple hydrographs and peak discharge magnitudes.

498   Generally, the most extreme or worst-case scenario is often selected by choosing the PMF

499   hydrograph with maximum discharge. In this section, we analyze the effects of PMF in terms of

500   flood inundation area by translating these hydrographs into flood inundation maps and

501   comparing the results to flood extents obtained from a conventional approach. This investigation

502   will improve the understanding of flood damages/extents resulting from a PMF event and

503   associated uncertainties.

504   The probabilistic flood maps are prepared as outlined in Section 2.3 and presented for each of

505   the 30 storms for CFSR-CT, CCSM4-BL, CCSM4-F1 and CCSM4-F2 (Figure 6, Panels a

506   through d for ME01, Panels e through h for ME02 and panels i through l for ME02R). The

507   results are presented in term of conditional probability of flooding for a given cell, assuming a

508   PMF has occurred for the region. Panel a and e also include the deterministic flood extents

509   obtained from Flood2D-GPU driven by conventional PMF, presented as white contours overlaid

510   on top of the probabilistic flood maps. In addition, the range of maximum flood inundation area

511   associated with each storm event is presented in Figure 7 for ME01 (Panel a), ME02 under

512   natural flow condition (Panel b) and ME02 under reservoir regulation (Panel c).

513   [Figure 6]

514   [Figure 7]

515   A comparison of maximum flood inundation extent for upstream domain (ME01; Figure 6a)

516   obtained from conventional approach (HMR based approach; 15.67 km^2) is very similar to

517   maximum flooding extents of CFSR-CT-ME01 (16.95 km^2) and CCSM4-BL-ME01(16.44 km^2)

518   resulting in an 8.2 % and 4.9% respective increment in inundation area compared to HMR. On

519   the other hand, the downstream domain (ME02; Figure 6 e) has a larger difference in flood

520   extents obtained from HMR approach (97.5 km^2) compared to maximum flood extents of CFSR-

521   CT-ME02 (118.5 km^2) and CCSM4-BL-ME02(102.08 km^2) resulting in a 21.5 % and 4.7%

522   respective increment in inundation area compared to HMR. A comparison of panels e and i in

523   Figure 6, reveals an overall effect of Allatoona reservoir in regulating flood damages in

524   immediately downstream areas. An ideal reservoir operation results in a decrease of maximum

525   flood inundation area by 9.5 % in case of CFSR-CT.

526   Under climate change, the projected maximum inundation area reveals a likely increase for

527   both near future period (CCSM4-F1) and far-future period (CCSM4-F2). The projected

528   maximum inundation area is computed as 17.44 km^2 and 19.24 km^2 respectively for ME01 which

529   suggests an increment of 7.9% and 17 % compared to maximum inundation area obtained for

530   baseline period CCSM4-BL-ME01 (Figure 7a). Similarly, an increase of 19.3% (22.4%) and

531   33.4% (45%) in the maximum inundation area is projected for ME02 (ME02R) for CCSM4-F1

532   and CCSM4-F2 respectively compared to the maximum flood inundation of 102.08 km^2 (88.87

533   km^2) for CCSM4-BL-ME02 (CCSM4-BL-ME02R). The results indicate that increase in

534   maximum inundation area is projected to be higher for ME02R compared to ME02. This

535   suggests that magnitude of storms in future time periods will change such that current reservoir

536   capacity will have lower efficiency to successfully mitigate flood damages downstream of the

537   region.

538   Given the wide range of areal extents produced for each storm set, a further insight into flood

539   characteristics (such as flood inundation area, gauge height etc.) with hydrologic/meteorological

540   parameters can improve the understanding of flood zones. The relationship between peak

541   discharge and maximum flood inundation area is presented in Figure 8. While the maximum

542   flood inundation area is directly related to the peak discharge at the outlet of each model domain.

543   The relationship is non-linear and positively correlated with higher variance observed for ME02

544   (Figure 8b) compared to ME01 (Figure 8a). This could be mainly attributed to the relatively flat

545   topography in ME02. The variability demonstrates that a similar peak discharge could result in

546   varying extents of flood inundation which could be attributed to hydrographs characteristics

547   (including timing, sequence and total flood volume) and spatial variations in streamflow. For

548   instance, two storms with maximum peak discharge of 11,112 m^3/s and 11,504 m^3/s respectively

549   produces a very different maximum flood inundation area of 102.8 km^2 and 82.01 km^2 for ME02

550   (Figure 8b).

551   Thus, reliance on a single peak discharge value for PMF obtained from the conventional

552   approach cannot capture such variations on flood impacts. This fact further highlights the

553   importance of ensemble-based approach over deterministic approach for a more comprehensive

554   understanding of flood damages resulting from an extreme event.

555   [Figure 8]

556   **3.4   Potential changes in flood impacts arising from PMF**

557   In this section, we employ the probabilistic flood maps to understand the potential changes in

558   flood regime and its impacts on infrastructure/urban developments under climate change. To

559   investigate how the conditional probability of flooding in a region changes in future, the

560   difference in probability of flooding is calculated for CCSM4-F1 and CCSM4-F2, with respect to

561   CCSM4-BL for each ME01, ME02 and ME02R. The grid cells either flooded (i.e. probability

562   =1) or non-flooded (i.e. probability =0) in inundation maps for each storm (CCSM4-BL,

563   CCSM4-F1 and CCSM4-F2) are excluded from analysis (Figure 9).

564   [Figure 9]

565   The results indicate that overall probability of flooding will increase by up to 30% in

566   CCSM4-F1 for each ME01, ME02 and ME02R, where most grid cells will observe an increase

567   in probability value ranging between 0–0.15. Similarly, the histogram for CCSM4-F2 indicate

568   that overall probability of flooding will increase by up to 60% for CCSM4-F2 for each ME01,

569   ME02 and ME02R with most cells observing a positive increase ranging between 0–0.25. This

570   process allows the identification of additional areas which may be more susceptible to flooding

571   in addition to the most vulnerable areas (i.e., probability =1). The analysis is further expanded to

572   demonstrate utility of probabilistic flood maps as a tool to identify potential hazards to electricity

573   grid infrastructure arising from PMF events in the downstream region of Allatoona Dam. The

574   electric substation data (Homeland Infrastructure Foundation-Level DATA (HIFLD); Figure 1)

575   overlaid on top of probabilistic flood maps reveal the probability of flooding for the grid cell

576   based on substation location. The individual results are presented in Figure 10. These results

577   identify the substations at high risk of flooding given a PMF event has occurred. Out of 23

578   substations selected for the analysis, 8 substations demonstrate a high probability of flooding

579   (>0.8) for ME02 under natural flow condition, which reduces to 3 substations under the effect of

580   ideal regulation from the reservoir for CCSM4-BL. Similarly, the substation which are currently

581   not at risk of flooding in CCSM4-BL but have a higher chance of flooding in future time periods

582   i.e. CCSM4-F1 and CCSM4-F2 are also identified (for instance, substation #8).

583   [Figure 10]

24

584   This risk identification can assist in improving current flood mitigation features while also

585   equips the decision makers with information to be utilized in strategic planning and development

586   of future urban areas/infrastructure.

587   **3.5   Sensitivity Analysis**

588   To understand the overall and relative sensitivity of flood inundation to various factors such

589   as meteorological forcings, climate change, hydraulics and hydrologic model inputs and

590   parameters; a comprehensive sensitivity test was performed with following sets of experiments.

591   (1) **Scenario 1–Baseline simulation (S1)**: One Flood2D-GPU simulation for ME02 driven

592   by hydrographs associated with the event with maximum peak discharge (out of 30

593   events) obtained from CCSM4 forcings (CCSM4-BL), and default Flood2D-GPU

594   configuration (i.e. 30 m grid resolution, and manning's n value = 0.035).

595   (2) **Scenario 2–Alternative meteorological forcings (S2)**:

596   **S2-a**: One Flood2D-GPU simulation for ME02 using PMF hydrographs with maximum

597   peak discharge obtained from CFSR forcings (CFSR-CT), and default Flood2D-GPU

598   configuration (i.e. 30 m grid resolution, and manning's n value = 0.035)

599   **S2-b**: One Flood2D-GPU simulation for ME02 using PMF hydrographs with maximum

600   peak discharge obtained from CFSR forcings (CFSR-CT), and default Flood2D-GPU

601   configuration (i.e. 30 m grid resolution, and manning's n value = 0.035)

602   (3) **Scenario 3–Climate change (S3)**:

603   **S3-a**: One Flood2D-GPU simulation for ME02 using PMF hydrographs with maximum

604   peak discharge obtained from near future CCSM4 forcings (CCSM4-F1), and default

605   Flood2D-GPU configuration (i.e. 30 m grid resolution, and manning's n value = 0.035)

606   **S3-b**: One Flood2D-GPU simulation for ME02 using PMF hydrographs with maximum

607   peak discharge obtained from far future CCSM4 forcings (CCSM4-F2), and default

608   Flood2D-GPU configuration (i.e. 30 m grid resolution, and manning's n value = 0.035)

609   (4) **Scenario 4–Horizontal grid resolution for Flood2D-GPU (S4)**: One Flood2D-GPU

610   simulation for ME02 driven by hydrographs associated with the event with maximum

611   peak discharge (out of 30 events) obtained from CCSM4 forcings (CCSM4-BL), and

612   default Flood2D-GPU configuration with 10-m DEM

613   (5) **Scenario 5–Manning's' roughness coefficient (S5)**:

614   **S5-a**: One Flood2D-GPU simulation for ME02 driven by hydrographs associated with

615   the event with maximum peak discharge (out of 30 events) obtained from CCSM4

616   forcings (CCSM4-BL), and default Flood2D-GPU configuration with manning's n value

617   = 0.015.

618   **S5-b**: One Flood2D-GPU simulation for ME02 driven by hydrographs associated with

619   the event with maximum peak discharge (out of 30 events) obtained from CCSM4

620   forcings (CCSM4-BL), and default Flood2D-GPU configuration with manning's n value

621   = 0.055.

622   (6) **Scenario 6–Antecedent moisture conditions (S6)**: One Flood2D-GPU simulation for

623   ME02 driven by hydrographs associated with the event with maximum peak discharge

624   (out of 30 events) obtained from CCSM4 forcings (CCSM4-BL), with unsaturated soil

625   moisture conditions at the beginning of hydrologic simulation, and default Flood2D-GPU

626   configuration (i.e. 30 m grid resolution, and manning's n value = 0.035)

627   (7) **Scenario 7–Reservoir operations (S7)**: One Flood2D-GPU simulation for ME02 driven

628   by hydrographs associated with the event with maximum peak discharge (out of 30

26

629   events) obtained from CCSM4 forcings (CCSM4-BL) adjusted to reflect ideal reservoir

630   operations and default Flood2D-GPU configuration (i.e. 30 m grid resolution, and

631   manning's n value = 0.035)

632 The simulation results from scenarios S2 through S7 are compared with reference to control

633 scenario (S1) in Figure 11. The relative sensitivity reveals that climate change (S3a and S3b) and

634 meteorological forcings (S2a) are the most sensitive factors for flood inundation area and the

635 median flood depths for ME02. The climate change is likely to cause a relative change of up to

636 33% (47.4%) in inundated area (median flood depth). These differences in inundation areas for

637 the above mentioned scenarios could be mainly attributed to changes in PMP values revealing

638 that precipitation is the most sensitive factor affecting flood regimes. The reservoir operations

639 (S7) can also contribute moderately by reducing the overall flood inundation area by

640 approximately 13% compared to S1. It is important to note that the reduction is calculated under

641 an ideal reservoir operation scenario and will be directly proportional to the maximum storage

642 capacity of reservoir as well. The other two sensitive parameters in this order include the effect

643 of antecedent moisture conditions in the hydrologic model (S6) and the effect of use of a high-

644 resolution DEM (S4). They produce a relative change of -8.2% and +6.7% respectively for the

645 inundation area. The effect of manning's roughness coefficient was found to be least sensitive in

646 this case. A similar trend is also noticed for median flood depths.

647   [Figure 11]

648

27

649 **4. Summary and Conclusions**

650   In this study, a high-resolution process-based hydro-meteorological modeling framework is

651   presented to generate ensemble based probabilistic flood maps for two selected domains in

652   Etowah Watershed, Georgia located in southeastern United States. These maps are prepared for

653   the worst-case flood scenarios i.e. PMF which occur under adverse set of hydrometeorological

654   conditions including PMP and other hydrologic factors such as saturated antecedent soil moisture

655   conditions. A total of 120 relative humidity maximized PMP storms were obtained under

656   historical and future climate conditions from Rastogi et al. (2017). These storms were used to

657   drive a calibrated hydrologic model (DHSVM) at a 90 m spatial resolution to generate PMF

658   estimates for the selected watershed. The high resolution 3-hourly hydrographs obtained from

659   DHSVM for each storm, were used to drive a two-dimensional GPU based hydraulic model

660   (Flood2D-GPU) at a 30 m spatial resolution to produce flood maps for each storm. The

661   probability of inundation is then calculated at each grid cell of flood domain, used to generate

662   probabilistic flood maps. Further, the relative sensitivity of flood inundation area and median

663   flood depth was evaluated for various factors such as meteorological forcings, climate change,

664   antecedent moisture conditions, and hydraulic model inputs and parameters.

665   The results indicate that peak discharge from the PMF hydrograph is likely to increase

666   significantly for the Etowah watershed region under a changing climate. The region downstream

667   of Allatoona Lake is likely to observe an increase of up to 58% in peak discharge magnitude for

668   near future period i.e. 2021-2050 (CCSM4-F1), and up to 109% for far future period i.e. 2071-

669   2100 (CCSM4-F2) under RCP8.5 compared to baseline period (CCSM4-CT). These changes in

670   PMF translate into approximately 19% and 33% increase in the flood inundation area. An

671   evaluation of probabilistic inundation maps reveal that the probability of flooding is likely to

672   increase by up to 30% and 60% respectively under the near future and far future scenarios

673   respectively. The relative sensitivity experiments further demonstrate that the precipitation is the

674   most sensitive factor affecting flood regime including flood inundation areas and depth. The

675   choice of meteorological forcings can contribute to up to a 16% change in the flood inundation

676   area. Further, the flood inundation elasticity relationships developed between peak streamflow

677   and corresponding flood inundation area reveals the uncertainties associated with the shape and

678   timings of hydrographs originating from the spatiotemporal variability in precipitation along

679   with the watershed heterogeneity.

680   This study presents a unique framework of high resolution process-based hydro-

681   meteorological and two-dimensional numerical flood model to enable generation of probabilistic

682   flood inundation maps through an ensemble-based approach for PMP and PMF estimation. The

683   uncertainties associated with the most sensitive factor i.e. precipitation and others can be

684   successfully captured with an ensemble approach as presented in this study. The comprehensive

685   relative sensitivity analysis and its effects on flood regime further identifies the most important

686   factors causing changes to flood regimes. Although, the study has focused on a particular

687   HUC08 basin, the framework can be extended to other regions to generate ensemble based

688   probabilistic flood inundation maps. These maps can serve as an important tool and provide

689   additional information to decision makers compared to deterministic inundation maps obtained

690   from conventional approach. Such an evaluation of a region not only determines the regions

691   under flood risks, but also informs the stakeholders about the probability of inundation to enable

692   an informed decision.

693

694

710

711

712 **References**

713 Alfieri, L., Salamon, P., Bianchi, A., Neal, J., Bates, P. and Feyen, L. (2014) Advances in pan-

714   European flood hazard mapping. Hydrological Processes 28(13), 4067-4077.

715 Alfonso, L., M. M. Mukolwe, and G. Di Baldassarre (2016), Probabilistic Flood Maps to Support

716   Decision-making: Mapping the Value of Information, *Water Resour. Res.*, *52*(2), 1026–1043,

717   doi:10.1002/2015WR017378.

718 Bates, P.D. and De Roo, A. (2000) A simple raster-based model for flood inundation simulation.

719   Journal of Hydrology 236(1-2), 54-77.

720 Beauchamp, J., R. Leconte, M. Trudel, and F. Brissette (2013), Estimation of the Summer-fall

721   PMP and PMF of A Northern Watershed under A Changed Climate, *Water Resour. Res.*, *49*,

722   3852–3862, doi:10.1002/wrcr.20336.

723 Büchele, B., H. Kreibich, A. Kron, A. Thieken, J. Ihringer, P. Oberle, B. Merz, and F. Nestmann

724   (2006), Flood-risk Mapping: Contributions Towards an Enhanced Assessment of Extreme

725   Events and Associated Risks, *Nat. Hazards Earth Syst. Sci.*, 6, 485–503, doi:10.5194/nhess-

726   6-485-2006.

727 Caseri, A., P. Javelle, M. Ramos, and E. Leblois (2016), Precipitation Ensembles for Flood Alert,

728   *J. Flood Risk Manage*, 9: 402-415. doi:10.1111/jfr3.12203.

729 Di Baldassarre, G., G. Schumann, P. D. Bates, J. E. Freer, and K. J. Beven (2010), Flood-plain

730   Mapping: A Critical Discussion of Deterministic and Probabilistic approaches, *Hydrol. Sci.*

731   *J.*, *55*(3), 364–376, doi:10.1080/02626661003683389.

732 Domeneghetti, A., S. Vorogushyn, A. Castellarin, B. Merz, and A. Brath (2013), Probabilistic

733   Flood Hazard Mapping: Effects of Uncertain Boundary Conditions, *Hydrol. Earth Syst. Sci.*,

734   *17*, 3127–3140, doi:10.5194/hess-17-3127-2013, 2013.

735 Federal Emergency Management Agency (FEMA) (2018), Guidance for Flood Risk Analysis

736 and Mapping; Hydrology: Rainfall-Runoff Analysis, https://www.fema.gov/media-library-

737 data/1520964160255-

738 7c49e1753d0b2634e0c5fb4999459374/Hydrologic_Rainfall_Runoff_Analysis_Feb_2018.pd

739 f, accessed May 2018.

740 Gangrade, S., S.-C. Kao, B. S. Naz, D. Rastogi, M. Ashfaq, N. Singh, and B. L. Preston (2018),

741 Sensitivity of Probable Maximum Flood in a Changing Environment, *Water Resour. Res.*, in

742 press, doi:10.1029/2017WR021987.

743 Giustarini, L., R. Hostache, D. Kavetski, M. Chini, G. Corato, S. Schlaffer, and P. Matgen

744 (2016), Probabilistic Flood Mapping Using Synthetic Aperture Radar Data, *IEEE T. Geosci.*

745 *Remote*, *54*(12), 6958–6969, doi:10.1109/TGRS.2016.2592951.

746 Interagency Advisory Committee on Water Data. (1982). "Guidelines for determining flood flow

747 frequency." Hydrology Subcommittee Bulletin 17B, U.S. Geological Survey, Office of

748 Water Data Coordination, Reston, VA, 194.

749 Jenkins, K., J. Hall, V. Glenis, and C. Kilsby (2017), A Probabilistic Analysis of Surface Water

750 Flood Risk in London, *Risk Analysis*, doi:10.1111/risa.12930.

751 Kalyanapu, A. J., S. Shankar, E. R. Pardyjak, D. R. Judi, and S. J. Burian (2011), Assessment of

752 GPU Computational Enhancement to A 2D Flood Model, *Environ. Modell. Softw.*, *26*(8),

753 1009–1016, doi:10.1016/j.envsoft.2011.02.014.

754 Klein, I. M., A. N. Rousseau, A. Frigon, D. Freudiger, and P. Gagnon (2016), Evaluation of

755 Probable Maximum Snow Accumulation: Development of A Methodology for Climate

756 Change Studies, *J. Hydrol.*, *537*, 74–85, doi:10.1016/j.jhydrol.2016.03.031.

757   Kunkel, K. E., T. R. Karl, D. R. Easterling, K. Redmond, J. Young, X. Yin, and P. Hennon

758   (2013), Probable Maximum Precipitation and Climate Change, *Geophys. Res. Lett.*, *40*,

759   1402–1408, doi:10.1002/grl.50334.

760   Micovic, Z., M. G. Schaefer, and G. H. Taylor (2015), Uncertainty analysis for probable

761   maximum precipitation estimates, *J. Hydrol.*, *521*, 360–373,

762   doi:10.1016/j.jhydrol.2014.12.033.

763   National Centers for Environmental Information (NCEI) (2018), U.S. Billion-Dollar Weather

764   and Climate Disasters, https://www.ncdc.noaa.gov/billions/, accessed May 2018.

765   Neal, J., C. Keef, P. Bates, K. Beven, and D. Leedal (2013), Probabilistic Flood Risk Mapping

766   including Spatial Dependence, *Hydrol. Process.*, *27*(9), 1349–1363, doi:10.1002/hyp.9572.

767   Nuswantoro, R., F. Diermanse, and F. Molkenthin (2016), Probabilistic Flood Hazard Maps for

768   Jakarta, *J. Flood Risk Manage*, *9*(2), 105–124, doi:10.1111/jfr3.12114.

769   Papaioannou, G., A. Loukas, L. Vasiliades, and G. Aronica (2016), Flood Inundation Mapping

770   Sensitivity to Riverine Spatial Resolution and Modelling Approach, *Nat. Hazards*, *83*(Suppl

771   1), 117–132, doi:10.1007/s11069-016-2382-1.

772   Papaioannou, G., L. Vasiliades, A. Loukas, and G. T. Aronica (2017), Probabilistic Flood

773   Inundation Mapping at Ungauged Streams Due to Roughness Coefficient Uncertainty in

774   Hydraulic Modelling, *Adv. Geosci.*, *44*, 23–34, doi:10.5194/adgeo-44-23-2017.

775   Pattison, I., S. N. Lane, R. J. Hardy, and S. M. Reaney (2014), The Role of Tributary Relative

776   Timing and Sequencing in Controlling Large Floods, *Water Resour. Res.*, *50*, 5444–5458,

777   doi:10.1002/2013WR014067.

778   Pedrozo-Acuña, A., J. P. Rodríguez-Rincón, M. Arganis-Juárez, R. Domínguez-Mora, and F. J.

779   González Villareal (2015), Estimation of Probabilistic Flood Inundation Maps for An

780   Extreme Event: Pánuco River, México, *J. Flood Risk Manage*, *8*(2), 177–192,

781   doi:10.1111/jfr3.12067.

782 Phillips, J. V., & Tadayon, S. (2006). Selection of Manning's roughness coefficient for natural

783   and constructed vegetated and non-vegetated channels, and vegetation maintenance plan

784   guidelines for vegetated channels in Central Arizona. US Department of the Interior, US

785   Geological Survey.

786 Prime, T., J. M. Brown, and A. J. Plater (2016), Flood Inundation Uncertainty: The Case of a

787   0.5% Annual Probability Flood Event, *Environ. Sci. Policy*, *59*, 1–9,

788   doi:10.1016/j.envsci.2016.01.018.

789 Rastogi, D., S.-C. Kao, M. Ashfaq, R. Mei, E. D. Kabela, S. Gangrade, B. S. Naz, B. L. Preston,

790   N. Singh, and V. G. Anantharaj (2017), Effects of Climate Change on Probable Maximum

791   Precipitation: A Sensitivity Study over the Alabama-Coosa-Tallapoosa River Basin, *J.*

792   *Geophys. Res.*, *122*, 4808–4828, doi:10.1002/2016JD026001.

793 Rousseau, A. N., I. M. Klein, D. Freudiger, P. Gagnon, A. Frigon and C. Ratté-Fortin (2014),

794   Development of A Methodology to Evaluate Probable Maximum Precipitation (PMP) Under

795   Changing Climate Conditions: Application to Southern Quebec, Canada, *J. Hydrol.*, *519*,

796   3094–3109, doi:10.1016/j.jhydrol.2014.10.053.

797 Smemoe, C. M., E. J. Nelson, A. K. Zundel, and A. W. Miller (2007), Demonstrating Floodplain

798   Uncertainty Using Flood Probability Maps, *J. Am. Water Resour. As.*, *43*(2), 359–371,

799   doi:10.1111/j.1752-1688.2007.00028.x.

800 Skamarock, W., J. Klemp, J. Dudhia, D. Gill, D. Barker, M. Duda, X. Huang, W. Wang and J.

801   Powers (2008), *A Description of the Advanced Research WRF version 3*, NCAR Technical

802   Note, NCAR/TN-475 STR125, National Center for Atmospheric Research, Boulder, CO.

803   Stratz, S. A. and F. Hossain (2014), Probable Maximum Precipitation in A Changing Climate:

804   Implications for Dam Design, *J. Hydrol. Eng.*, *19*(12), 06014006,

805   doi:10.1061/(ASCE)HE.1943-5584.0001021.

806   United Nations Organization (1964), Manual of Standards and Criteria for Planning Water

807   Resource Project, Water Resource Series, 26.

808   Wing, O.E.J., Bates, P.D., Sampson, C.C., Smith, A.M., Johnson, K.A. and Erickson, T.A.

809   (2017) Validation of a 30 m resolution flood hazard model of the conterminous United

810   States. Water Resources Research 53(9), 7968-7986.

811   Wigmosta, M. S., L. W. Vail, and D. P. Lettenmaier (1994), A Distributed Hydrology-vegetation

812   Model for Complex Terrain, *Water Resour. Res.*, *30*(6), 1665–1679,

813   doi:10.1029/94WR00436.

814   Wigmosta, M. S., B. Nijssen, P. Storck, and D. P. Lettenmaier (2002), The Distributed

815   Hydrology Soil Vegetation Model, in *Mathematical Models of Small Watershed Hydrology*

816   *and Applications*, V.P. Singh, D.K. Frevert, eds., Water Resource Publications, Littleton,

817   CO., p. 7–42.

818   World Meteorological Organization (WMO) (2009), *Manual on Estimation of Probable*

819   *Maximum Precipitation (PMP)*, WMO-No. 1045, World Meteorological Organization,

820   Geneva, Switzerland.

821   Zischg, A. P., G. Felder, R. Weingartner, N. Quinn, G. Coxon, J. Neal, J. Freer, and P. Bates

822   (2018), Effects of Variability in Probable Maximum Precipitation Patterns on Flood Losses,

823   *Hydrol. Earth Syst. Sci.*, *22*, 2759–2773, doi:10.5194/hess-22-2759-2018.

824

Figures and Tables
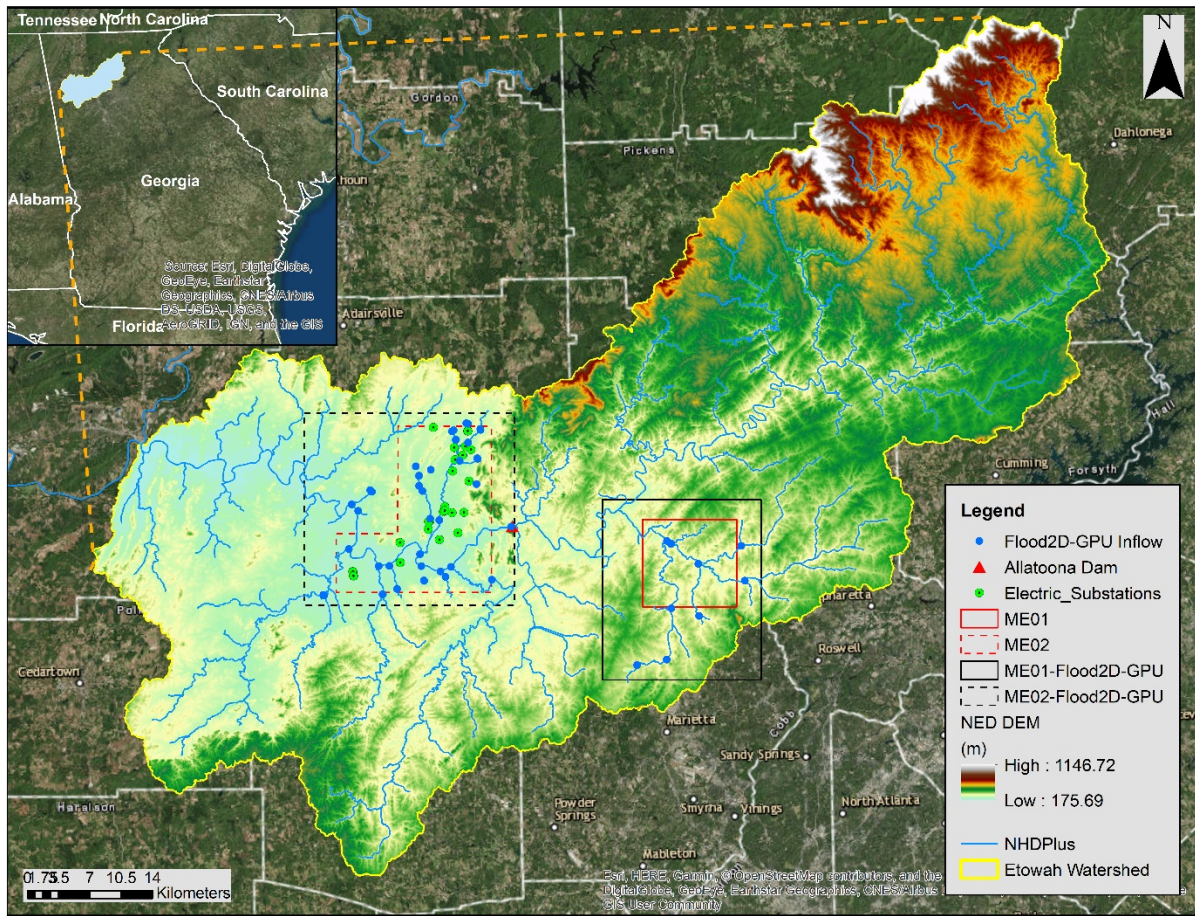
827
828 **Figure 1.** Etowah watershed with two selected areas of interest: ME01 and ME02; along with
829 Flood2D-GPU setup including computational domains, DEM, inflow locations and stream
830 network. The inserted panel at left shows the overall location of Etowah Watershed in the state
831 of Georgia, United States.
832
833
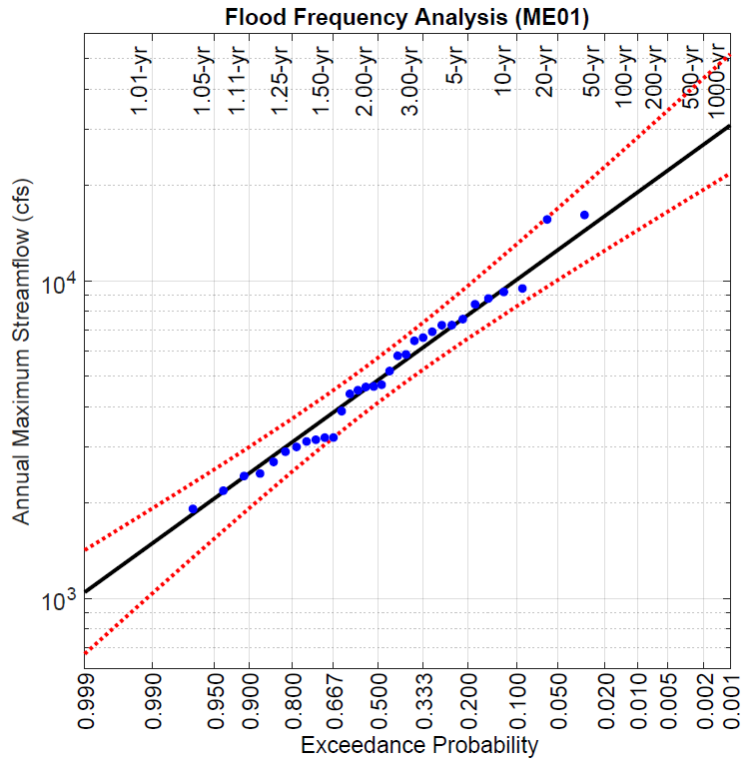
**Figure 2.** Standard flood frequency analysis for ME01 as per the guidelines of Bulletin 17B.
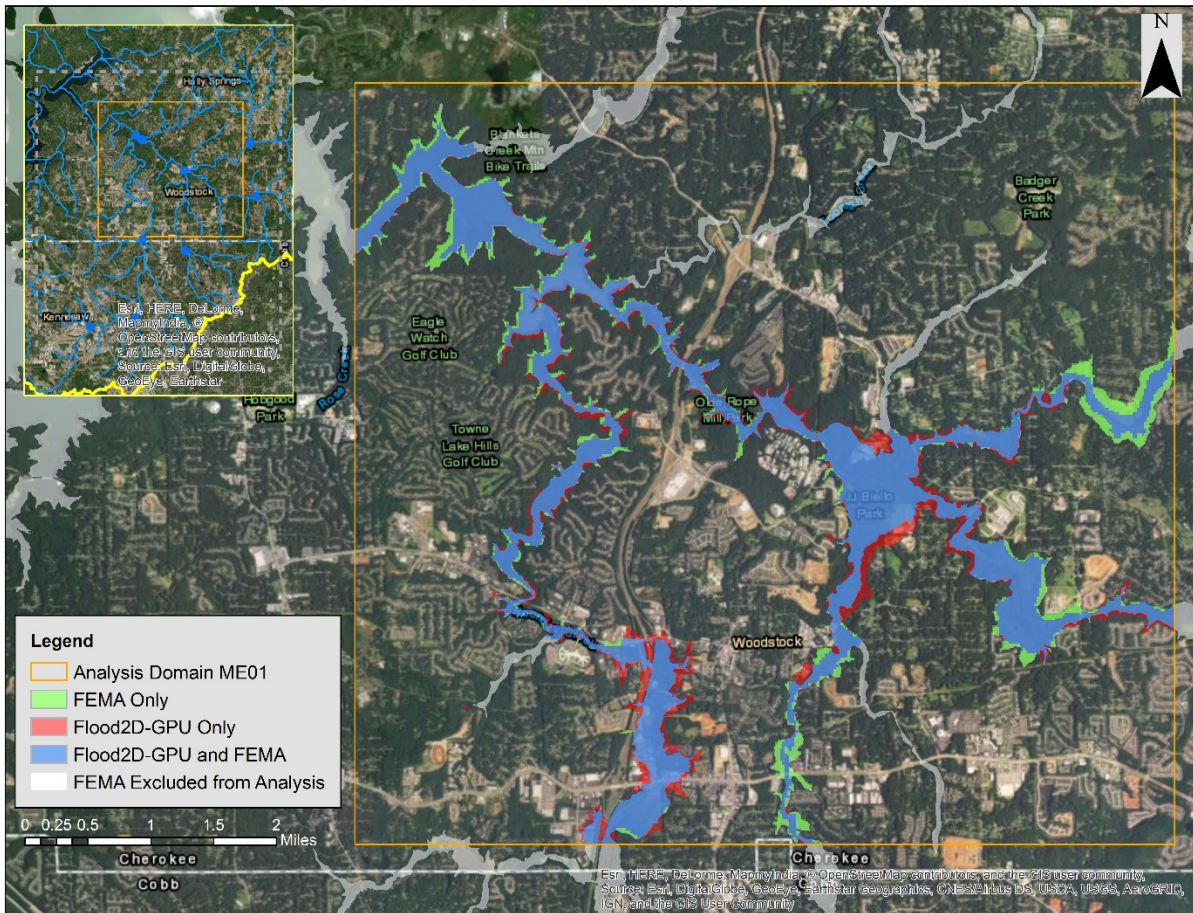
838
Figure 3. A comparison of flood inundation spatial extents obtained from Flood2D-GPU and
FEMA for 100-year flood event. The regions flooded with both Flood2D-GPU and FEMA flood
zones are presented in blue. The region in red/green represent the cells flooded only by Flood2D-
GPU/FEMA.

843
844
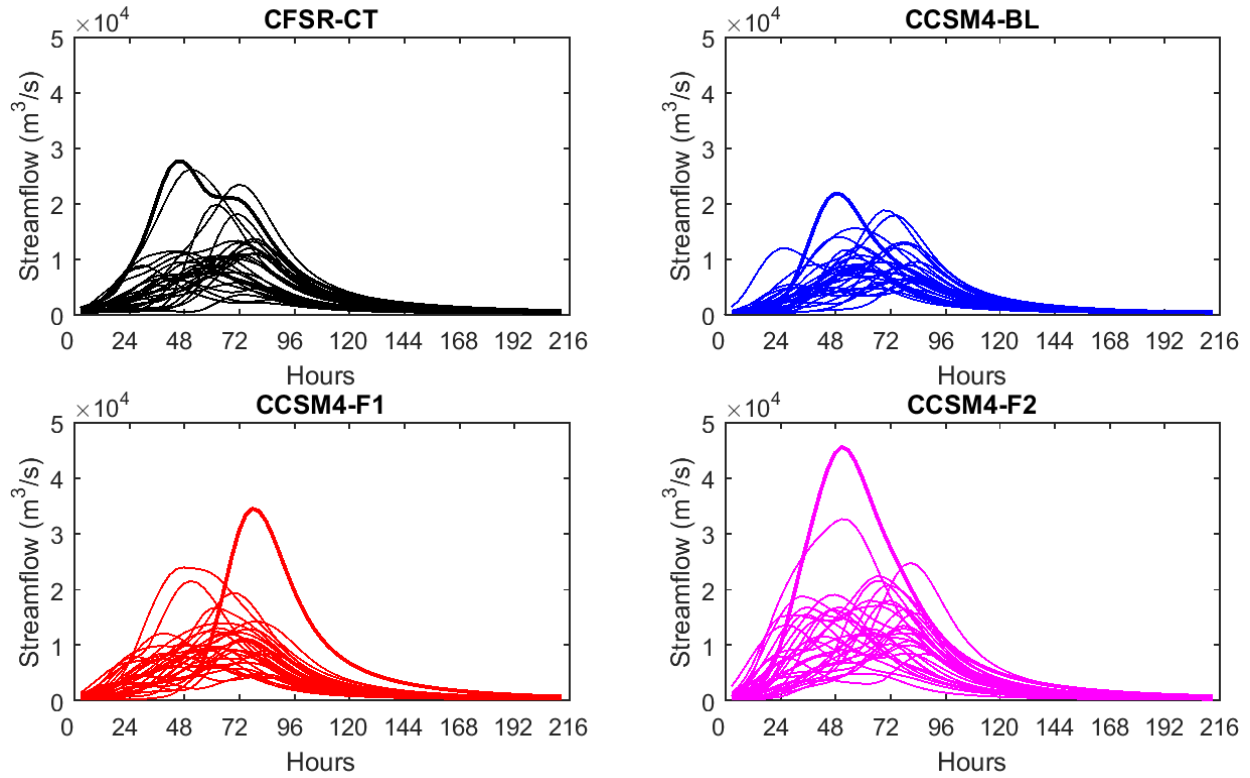
845
Figure 4. Ensemble PMF hydrographs for each set of PMP storms (CFSR-CT, CCSM4-BL,
CCSM4-F1, and CCSM4-F2) at the outlet of Etowah Watershed. The hydrograph resulting in
peak discharge is presented as a thick line.

849
850
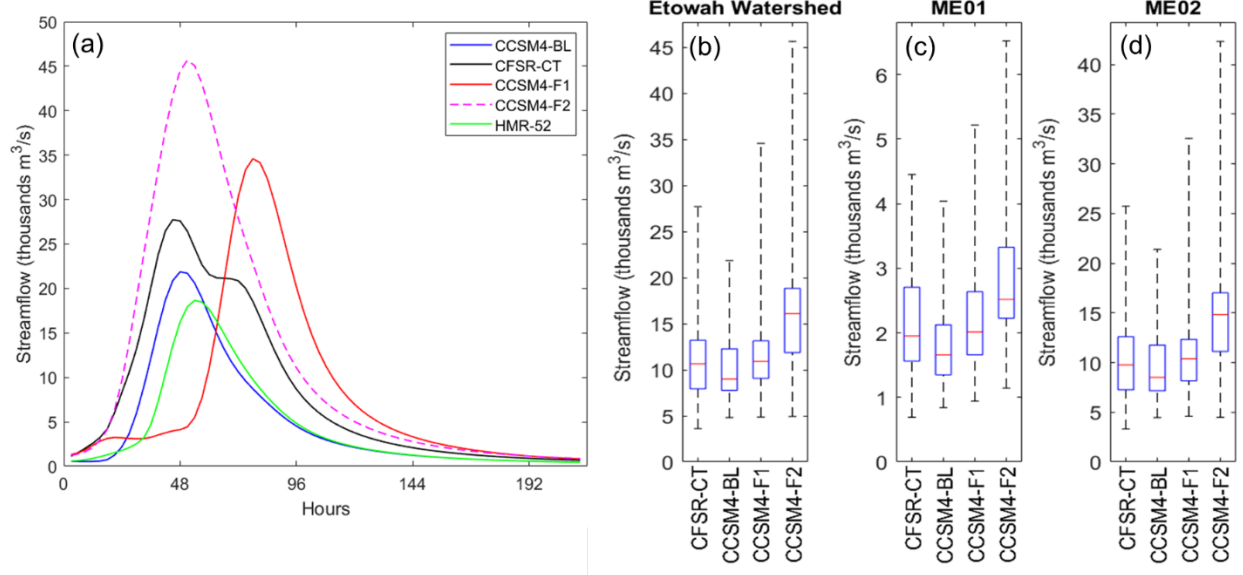
851
852 **Figure 5.** PMF Hydrographs selected based on peak discharge for Etowah Watershed (Panel a)
853 and range of peak discharge for each set of simulations (CFSR-CT, CCSM4-BL, CCSM4-F1,
854 and CCSM4-F2) for Etowah Watershed and ME01 and ME02 (Panel b, c and d respectively).
855
856
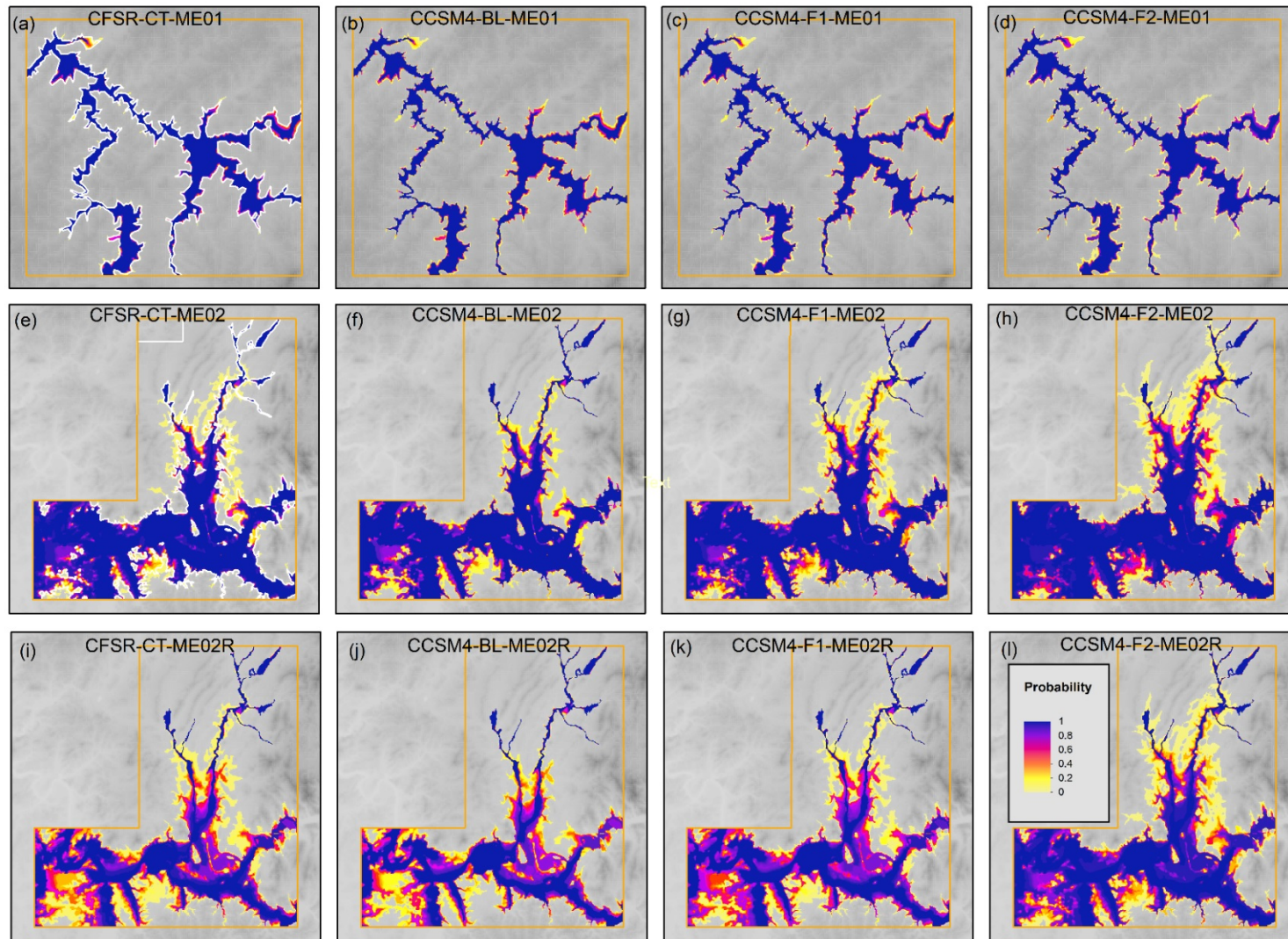
Figure 6. Probabilistic flood maps for ME01 (a through d), ME02 (e through h), ME02 with reservoir regulation (i through m) for each of the storm sets CFSR-CT, CCSM4-BL, CCSM4-F1 and CCSM4-F2. The Panels a and e also show HMR52 based flood extents in white contour.
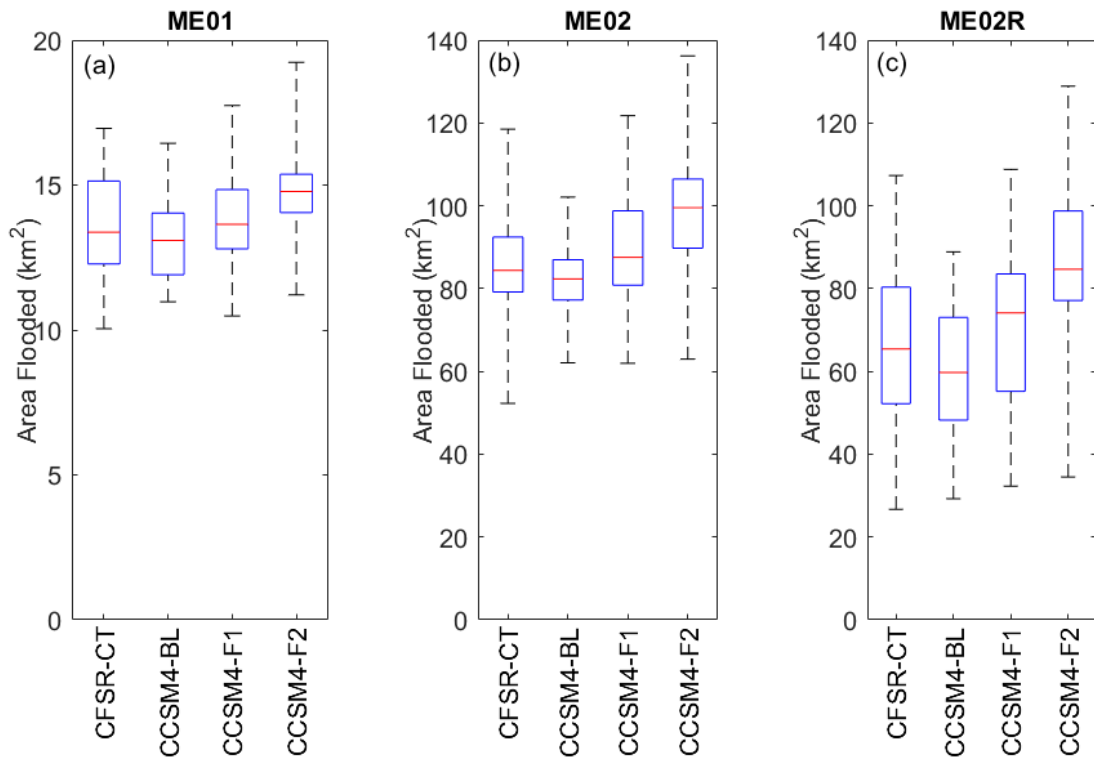
862
863 **Figure 7.** Boxplot showing the range of area under inundation for each of the storms sets for
864 region ME01 (Panel a), ME02 under natural flow condition (Panel b) and ME02 under reservoir
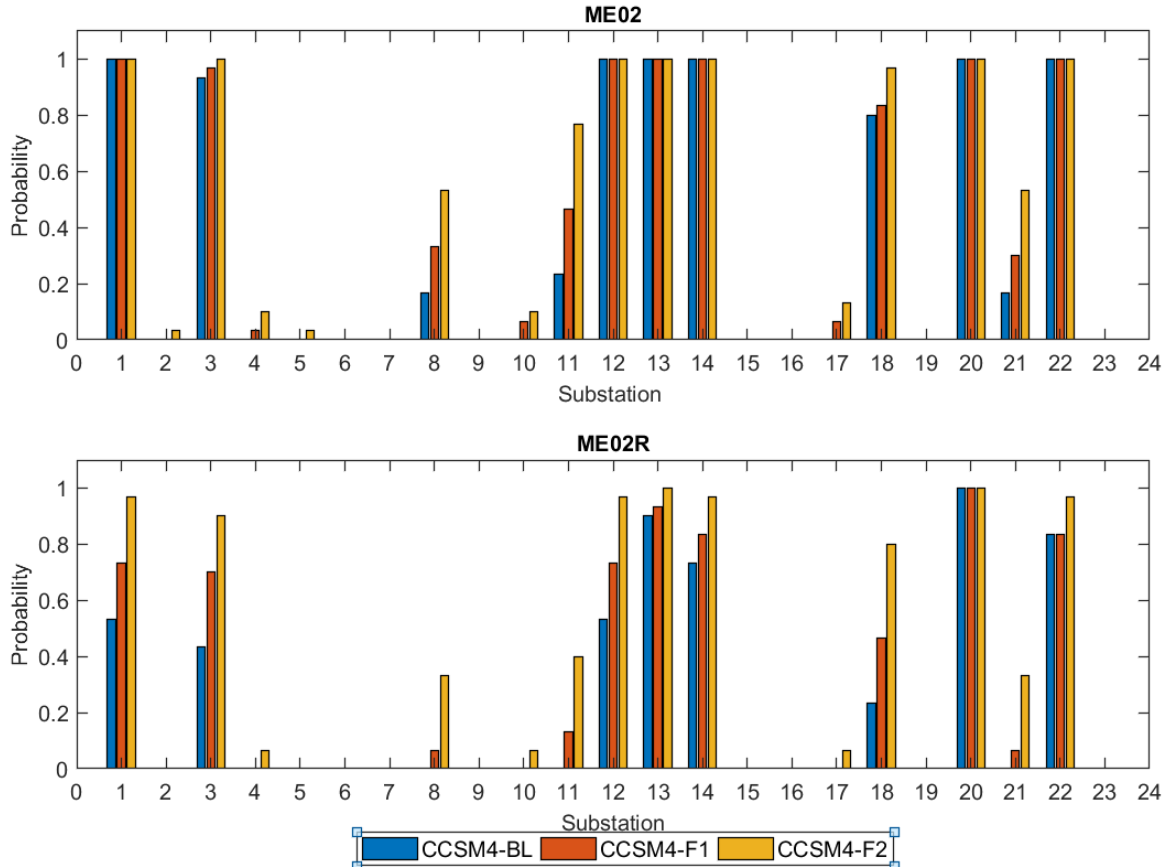865 regulation (Panel c).
866
867
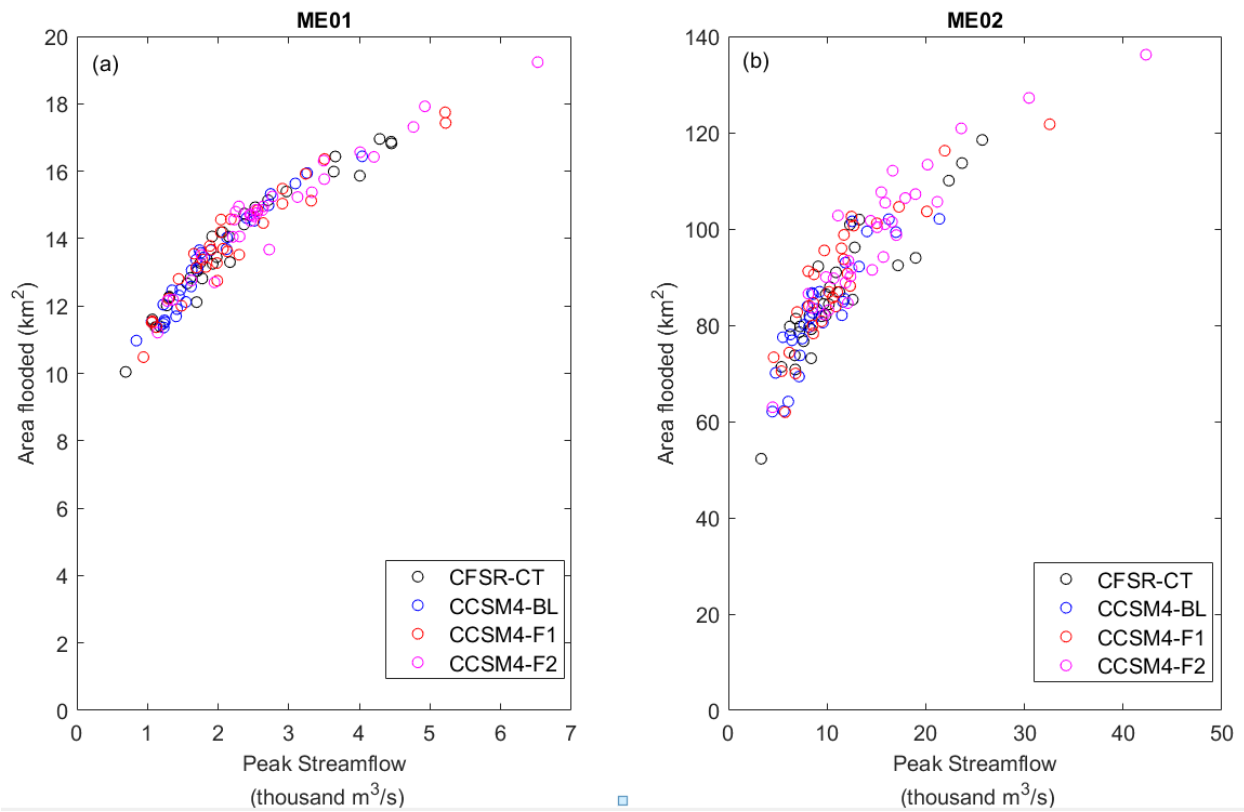
Figure 8. Flood inundation elasticity with respect to peak discharge for each set of simulations (CFSR-CT, CCSM4-BL, CCSM4-F1, and CCSM4-F2) for ME01 and ME02.
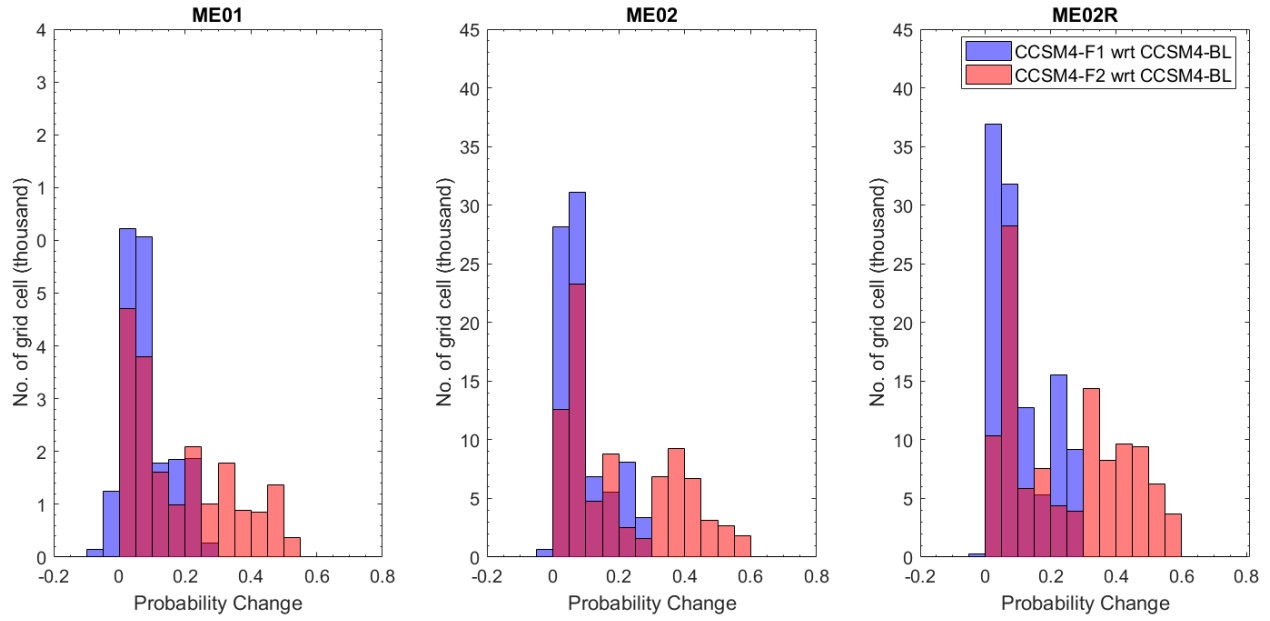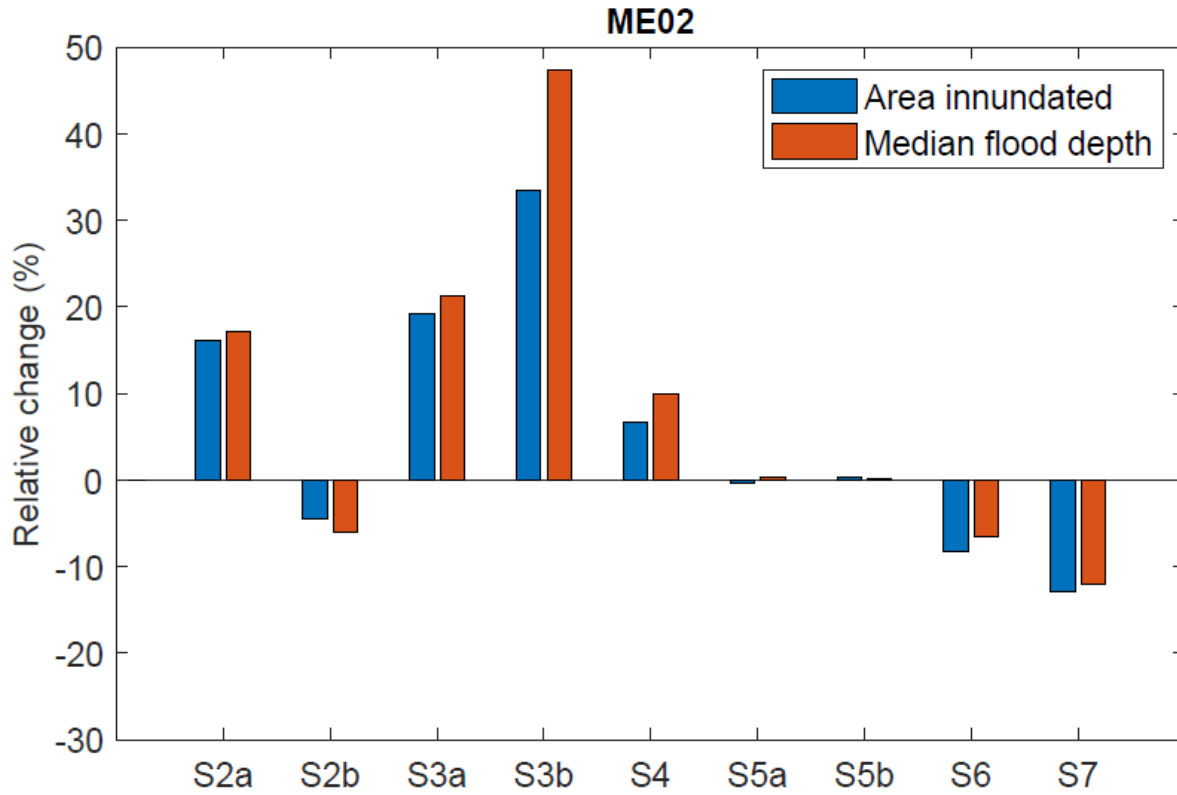
873
874 **Figure 9.** Changes in flood inundation probability for near future (CCSM4-F1) and far future
875 (CCSM4-F2)
876
877

Figure 10. Probability of flooding for 23 selected substations for each storm set i.e. CCSM4-BL, CCSM4-F1 and CCSM4-F2 for ME02 under natural flow (panel a) and under ideal reservoir regulation (panel b).

Figure 11. Figure summarizing relative sensitivity of area inundated and median flood depths from each scenario with reference to scenario 1 (S1). The relative change is calculated by comparing the percent change of the given variable with reference to control scenario (S1).

890 **Table 1.** Contingency Table for the analysis domain in ME01 represented as a fraction of total
891 number of cells in the analysis domain.

Cells	Wet in Model (M1)	Dry in Model (M0)
Wet in FEMA (B1)	0.0798 (M1B1)	0.0181 (M0B1)
Dry in FEMA (B0)	0.0142 (M1B0)	0.8880 (M0B0)

892
893

894 **Table 2.** Key flood model performance metrics calculated for ME01 for a 100-year ensemble
895 flood event. Adopted from Wing et al. (2017) .

Criterion	Formula	Calculated Value	Range	Description
Hit Rate (H)	M1B1 / (M1B1+M0B1)	0.82	0 - 1 0 = (none of the wet benchmark data are wet model data) 1 = (all of the wet benchmark data are wet model data).	Measure of tendency of model to accurately predict the benchmark flood extents
False Alarm Ratio (F)	M1B0 / (M1B0+M1B1)	0.15	0 – 1 0 (no false alarms) 1 (all false alarms).	Measure of tendency to overpredict flood extent
Critical Success Index (C)	M1B1 / (M1B1+M0B1 +M1B0)	0.71	0 - 1 0 (no match between modeled and benchmark data) 1 (perfect match between modeled and benchmark data).	Measure of fit with penalty for overprediction and underprediction
Error (E)	M1B0 / M0B1	0.78	0 – infinity E=1: no bias, 0<=E<1 indicates a tendency toward underprediction, and 1<E<=infinity indicates a tendency toward overprediction.	Measure of tendency toward overprediction or underprediction.

896